Light Ion Mass Spectrometer for space-plasma investigations

David L. Reasoner, Charles R. Chappell, Stanley A. Fields, and William J. Lewter

NASA/Marshall Space Flight Center, Marshall Space Flight Center, Alabama 35812

(Received 14 July 1981; accepted for publication 14 December 1981)

Recent studies of the low-energy plasma population in the Earth's space environment have revealed that this plasma population is much more complex than previously supposed and that a simple model of ionospheric evaporation cannot explain the distributions. There was a need to develop an advanced instrument to study this plasma in detail, and this paper describes the scientific background, design, development, and in-flight characteristics of such an instrument, the Light Ion Mass Spectrometer (LIMS). This instrument combines a magnetic mass spectrometer, a planar-grid retarding potential analyzer, and multidirectional sensor heads to measure the mass composition, density, temperature, and flow velocity of low-energy ($E<100$ eV) plasma. The studies which were conducted leading to the final design will be discussed in detail and will illustrate certain effects which arose in the combining of energy and mass analysis into a single sensor. The instrument was flown on a high-altitude satellite in February 1979, and selected flight data will be presented to demonstrate the instrument performance.

PACS numbers: 07.75. + h, 94.20. − y

INTRODUCTION

The environment surrounding the Earth where matter exists mostly in an ionized state and the Earth's magnetic field exerts a strong influence upon the particle motions is called the magnetosphere. Although its existence had been suspected for some years because of sensible manifestations such as the aurora and the effects upon radio communications, no comprehensive study was possible until the advent of artificial Earth satellites in the late 1950's. From the very first measurements with *in situ* instruments, advances in space physics research have followed advances in spacecraft technology and instrumentation techniques which allowed more sophisticated measurements of plasmas, magnetic fields, and electromagnetic waves.

Near the Earth, the ionosphere is at the interface between the upper atmosphere and magnetosphere and is characterized by a transition from particle motions controlled by neutral gas dynamics to particle motions controlled by interaction of ions and electrons with magnetic and electric fields. The plasmasphere is a region in the inner magnetosphere of low-energy, or "cold" plasma, which originates from the upward motion of ionospheric particles, a process known as plasmaspheric filling.

In the 1960's and early 1970's direct satellite measurements and ground-based electromagnetic wave probing techniques gave a comprehensive view of the density distribution of the cold plasma population in the Earth's magnetosphere.[1-3] There were, however, no direct measurements of the low-energy plasma mass composition, temperature, density, pitch-angle distribution (distribution relative to the magnetic field direction), or plasma flow velocity. Such measurements are crucial to studies of the mechanics of plasma interchange between the ionosphere and plasmasphere.

This paper describes the evolution and development of an instrument, the Light Ion Mass Spectrometer (LIMS), designed to make these important low-energy plasma measurements. The instrument was developed for flight on the joint Department of Defense/National Aeronautics and Space Administration spacecraft SCATHA, a satellite to study *Satellite Charging At High Altitudes*. This satellite, whose primary mission was to study spacecraft–plasma interactions and electrostatic charging, was launched into a near-geosynchronous orbit which is an excellent position to study the outer plasmasphere and the low-energy plasma population on magnetic-field lines connecting to the auroral regions.

Following the Introduction, the design requirements will be discussed, followed by descriptions of the analyses used to select the final design, the calibration procedures, and the flight configuration. Some examples of flight data will be shown which will illustrate the instrument capabilities.

I. DESIGN PARAMETERS AND SPECIFICATIONS

The LIMS design was dictated by estimates of the characteristics of the plasma population which was to be studied. The upper ionosphere is principally composed of hydrogen, helium, and oxygen with an extremely strong altitude dependence of the relative composition.[4] Therefore, a prime requirement of the LIMS instrument was the ability to discriminate ions according to their mass, and hence their species. Previous studies by other spacecraft[5] had indicated that in many cases the so-called "cold" plasma component at high altitudes was significantly more energetic than the thermal ionospheric plasma from which it originated. This required that the LIMS be able to measure the ion energy distribution. The third primary requirement arose from previous ob-

servations of strong anisotropies in the plasma distributions.[6] This required the LIMS to have directional discrimination.

The requirements for the LIMS were then that the instrument be able to discriminate among the ions H^+, He^+, and O^+; be able to measure ion energies from essentially 0 up to 100 eV; be able to sample the plasma distribution in multiple directions; and, finally, possess a dynamic range sufficient to measure ion densities from 0.1 ion/cm^3 up to 1000 ions/cm^3.

II. DESIGN OF THE LIMS

The choice of methods for particle energy discrimination is in large measure dictated by the particle energy of interest. For high particle energies ($E > 100$ keV) direct measurement by measuring the total energy deposited as the particle is stopped in a detector is commonly used. At lower energies, however, where inherent detector noise limits resolution and sensitivity, energy sorting by electrostatic or magnetic fields is often employed. The retarding potential analyzer, or RPA, technique was chosen for the LIMS for two primary considerations. The first was that at the very low plasma densities and temperatures expected, the *differential* flux would have become small in the limit of very low energies. The second consideration was similarly concerned with sensitivity in that it was desirable to provide particle acceptance over as wide an angle range as possible, preferably ±90°. The planar-grid RPA answers both considerations in that it inherently provides an integral measurement and at the same time the acceptance angle can be made very large, approaching ±90°.

There have been many techniques developed to measure ion mass, and the literature on the subject is extensive. Many mass-spectrometer techniques are based on the principle that ions of the same kinetic energy have a velocity and momentum which is a function of mass. Ions are produced with a uniform energy either by accelerating a thermal-ion population with an accelerating potential or by energy selection from an existing energetic population. The ions are separated according to either their velocity or momentum, which effectively produces a separation according to mass.

Examples of velocity-selection mass analyzers are the Bennett Radio Frequency Spectrometer[7] and the Quadrupole Analyzer.[8] The Bennett analyzer uses a planar-grid arrangement and combinations of static and radio-frequency potentials for ion mass separation. The Quadrupole Analyzer uses the concept of mass-dependent trajectories to effect separation according to mass. Momentum-selection analyzers use magnetic fields either singly or in combination with electrostatic fields. There are advantages and disadvantages to each type of analyzer. The Bennett and Quadrupole Analyzers do not involve magnetic material and hence are, in general, of lower weight and do not produce stray magnetic fields, possible areas of concern for spacecraft missions. However, these analyzers require radio-frequency potentials,

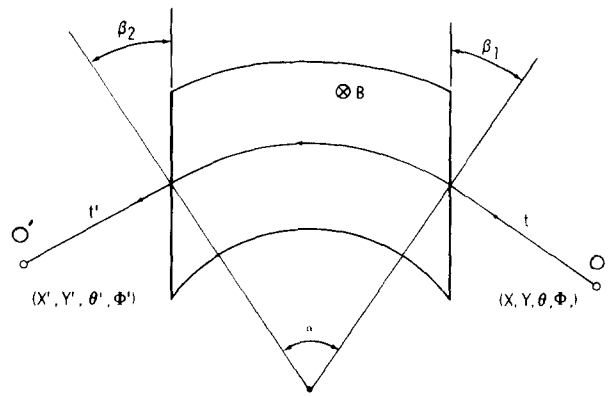

FIG. 1. Geometry of a deflection magnet system.

and the electronic circuitry tends to be complex. Magnetic analyzers can cause problems due to weight and magnetic-field contamination, but these problems can be overcome by careful attention to the magnetic circuit design. The magnetic analyzer concept was selected for the LIMS design, and we now turn to a discussion of the design parameters.

Conceptually, a magnetic-focusing mass spectrometer separates ions according to their magnetic rigidity defined as

$$R = Br_c = mv/q, \tag{1}$$

where q is the ion charge, B is the magnetic field strength, and r_c is the radius of curvature of the trajectory in the magnetic field. For a suitable arrangement of magnet pole faces and collimating apertures, only those ions whose momentum-to-charge ratio, m/q, satisfies the equation above will be transmitted through the spectrometer.

If V_{pa} is an accelerating potential applied to ions initially at zero energy prior to entry into the spectrometer, we have

$$Br_c = \left(\frac{2mV_{pa}}{q}\right)^{1/2} \tag{2}$$

with the final result that for a given value of accelerating potential V_{pa}, only those ions with the proper mass-to-charge ratio, m/q, will be passed through the spectrometer and subsequently detected.

An alternate viewpoint is that a magnetic field configuration is a "magnetic lens," with certain focusing properties. An elegant treatment by Penner[9] provides a matrix formulation method for calculating ion focusing in several types of magnetic-field configurations. The case of interest here is that of the uniform field magnet with parallel pole faces. The geometry for the general case is illustrated in Fig. 1. In the coordinate system shown, all quantities are referenced to the central ray indicated by the line with arrows. The entrance aperture is located at 0 and the exit aperture at 0'. x and θ are the perpendicular displacement and angle from the central ray in the plane of the paper and y and ϕ are displacements out of the plane of the paper. The quantities x', y', θ', and ϕ' are the corresponding quantities measured at the exit point

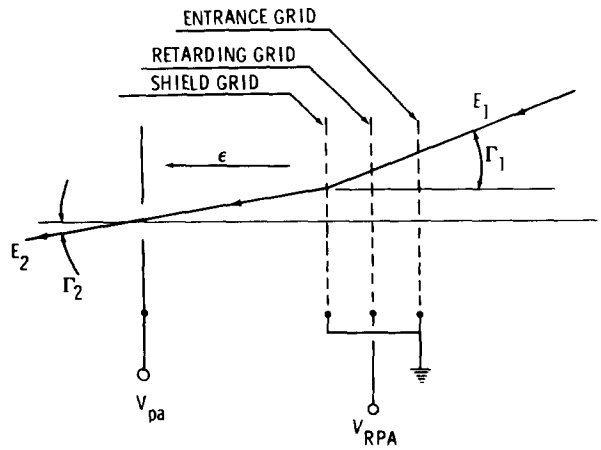

FIG. 2. Geometry of a retarding grid system coupled to a post-acceleration system.

0′. The quantities t and t' are the distances from the entrance and exit apertures to the respective pole edges. α is the angle through which the central ray is deflected and β_1, β_2 are the angles between the pole edges and the central ray at the points of entry to and exit from the magnetic field. The transformations from the unprimed quantities to the primed quantities are rather complex and can be found in Penner.[9] For our purposes we are interested in finding values of α, β_1, and β_2 which make x' and $y' = 0$ for $x = y = 0$, regardless of the values of θ and ϕ. This is the condition for focusing; all particles passing the entrance aperture regardless of angle will be focused back to the exit aperture. For purposes of symmetry we set $\beta_1 = \beta_2$ and $t = t'$. Multiplying out the transformations referenced above and setting $x' = y' = x = y = 0$, we obtain the equations

$$0 = 2t_x \frac{\cos(\alpha - \beta)}{\cos\beta} + r_c \sin\alpha + t_x^2 \frac{(\tan^2\beta - 1)\sin(\alpha - 2\beta)}{r_c \cos 2\beta} \quad (3)$$

$$0 = 2t_y(1 - \alpha\tan\beta) + \alpha r_c + \frac{t_y^2(\alpha\tan^2\beta - 2\tan\beta)}{r_c}, \quad (4)$$

where the separate equations for t_x and t_y reflect that, in general, there are differing focal distances in the two planes.

It is instructive to examine some limiting cases. The solutions for t_y are

$$t_y = r_c/\tan\beta, \quad (5a)$$

$$t_y = \frac{r_c\alpha}{\alpha\tan\beta - 2}, \quad (5b)$$

and for $\beta = 0$ (central ray normal to the pole edges) one solution for t_y is negative and the other becomes infinite. Thus, there is no focusing in the y direction. By contrast, in the x direction (setting $\beta = 0$) we obtain for a positive solution

$$t_x = r_c\left(\frac{1 - \cos\alpha}{\sin\alpha}\right). \quad (6)$$

Two cases of special interest historically are for $\alpha = 90°$, giving $t_x = r_c$, and $\alpha = 180°$, giving $t_x = 0$. In the latter case, the focus points are located at the pole edges, while in the former the focal distance is equal to the radius of curvature of the central ray.

It is always possible to obtain focusing in the plane perpendicular to the magnetic field (the $x - \theta$ plane) for $\beta = 0$ by selecting t_x, α, and β so that Eq. (6) is satisfied. Focusing in the $y - \phi$ plane is, however, possible only if $\beta \neq 0$; that is, if the pole edges are not perpendicular to the central ray. We shall consider these implications in greater detail later.

Before proceeding further with a discussion of the magnet design, it is necessary to consider the effects of the combination of the planar-grid RPA for energy analysis and of the magnetic spectrometer for mass analysis. As will be seen, there are important considerations which appear in the combination which are of no concern when considering either analyzer individually.

The geometry of the RPA grid assembly and the mass-spectrometer entrance aperture is shown in Fig. 2. The retarding grid is placed between the entrance grid and the shield grid, with the latter two grids at the local reference ground potential. The post-acceleration potential provides an equal increment of kinetic energy per unit charge to all ions which have sufficient initial energy to overcome the retarding potential and reach the shield grid. This acts to transform ions in energy-angle coordinates E, Γ from initial values E_1 and Γ_1 to final values E_2 and Γ_2. The ions enter the mass analyzer with angle Γ_2, which is related to Γ_1 according to

$$\Gamma_2 = \tan^{-1}\left(\frac{E_1\sin^2\Gamma_1}{E_1\cos^2\Gamma_1 + qV_{pa}}\right)^{1/2}. \quad (7)$$

Whereas the RPA has azimuthal symmetry around the central ray, the magnetic focusing spectrometer does not. The focal lengths t_x and t_y are, in general, different in the two planes, and for certain simple geometries there is no focusing in the y direction. The RPA alone has a response that is independent of the initial particle energy (for $E_1\cos^2\Gamma_1 > V_{pa}$) and the arrival angle Γ_1. The combination of the RPA and the magnetic focusing spectrometer will not be equally sensitive to all incident particles which pass through the RPA but rather will discriminate according to initial energy and arrival direction. Even for a magnet geometry which has equal focal lengths in directions parallel and transverse to the magnetic field, there are physical limits to the maximum angle θ or ϕ which a particle can depart from the central ray at the entrance aperture and still be transmitted to the exit aperture. Requirements for a finite magnet pole spacing, magnetic shielding, and internal baffling to attenuate scattering of solar ultraviolet photons and high-energy particles all combine to limit this angle by placing physical barriers in the particle trajectory paths.

In the course of the design a trade study was done to examine the relative merits of first-order focusing only (focusing in the plane perpendicular to the magnetic field only) vs first- and second-order focusing (focusing in both planes with $t_x \approx t_y$). For first-order focusing only at $\alpha = 90°$ Eqs. (5) and (6) show that $t_x = r_c$ and $t_y \to \infty$. For second-order focusing, $\beta_1 = \beta_2 \neq 0$, and Eqs. (3) and (4) were evaluated numerically for various values of t_x and t_y searching for values which made $t_x \simeq t_y$ with an auxiliary criterion that t_x and t_y not become significantly larger than r_c in order that the physical size of the analyzer not become excessive. The numerical analysis showed that for a selection of $\alpha = 100°$ and $\beta = 35°$, $t_x \approx t_y = 2.03 r_c$. The advantage of second-order focusing is gained only at the expense of a longer focal length which acts to decrease the analyzer throughput unless all dimensions are scaled proportionally. To do so, however, would have required significant increases in weight and volume. This option was not available and the net effect of selecting first- and second-order focusing over first-order focusing only would have been an increase in the overall instrument sensitivity by a factor of 2. This was not considered to be sufficient justification to undertake a second-order focusing design, particularly when the increased complexity of the magnet and yoke was considered. The final selection then was a 90° sector magnet with first-order focusing only and a radius of curvature r_c of 3 cm.

The final aspect of the instrument design involved the selection of a particle detector. A channel electron multiplier was chosen because of its high efficiency for detection of ions[10] and for its relatively small size. This last was important since the expected orbit of the host satellite would be within the outer Van Allen radiation belt and it was necessary to provide localized shielding in order to reduce the background signal due to high-energy penetrating particles. The channel multiplier configuration chosen was a standard C-shaped 1-mm-diam unit with a 3-mm-diam entrance aperture. A brass shield surrounded the entrance aperture and the first 1/3 of the multiplier length to provide the required radiation shielding. The multiplier was biased with the output at ground potential and the entrance aperture at −2600 V. The multiplier entrance was the most negative point in the system, thereby providing a focusing effect and increased detection efficiency for positive ions. A second beneficial aspect of this biasing method was that any secondary electrons created within the instrument either by ion bombardment or by scattered solar ultraviolet photons were repelled away from the multiplier and did not contribute to the background signal level.

Figure 3 is a sketch of the sensor ion optics. The entrance grid and shield grid are maintained at ground potential as discussed above. Ions accelerated by the post-acceleration potential, V_{pa}, pass through the mass analyzer entrance aperture, travel along a field-free drift path, and enter the magnetic field. Those exiting the magnet along the proper trajectory pass through the exit aperture and impinge upon the channel multiplier detector. The grids were fabricated of electroformed mesh mounted between annular rings. The magnetic field was generated by samarium–cobalt magnet sections totally enclosed within a soft iron yoke. The magnetic field strength was 1500 G. The radius of curvature of the central ray was 3.0 cm, which was also the distance from the entrance and exit apertures to the pole edges. The entrance aperture area was 0.01 cm^2. The grids were 5.0 cm in diameter with a spacing of 0.3 cm grid to grid.

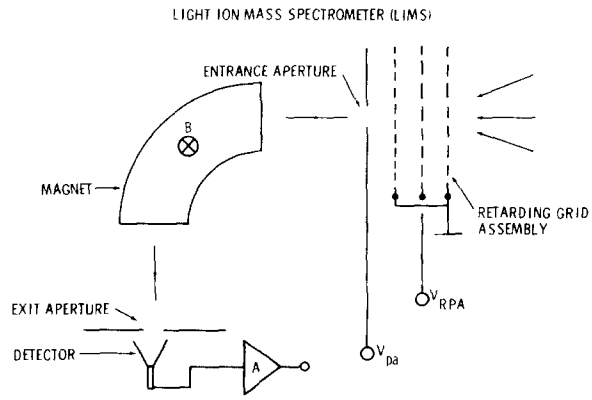

FIG. 3. Sketch of the ion optics of the LIMS sensor. Relevant dimensions are given in the text.

III. CALIBRATION

The task of calibration of the LIMS was divided into four areas. These were to determine the location and width of the mass transmission functions, to verify the operation of the retarding potential analyzer, to determine the solid angle response of the instrument as a function of energy, and to determine the effective area A_e, a quantity which represents the combined effects of entrance aperture area, grid transmission, particle detector efficiency, and losses due to baffles and fringing fields.

All calibration activities required a stable source of low-energy ions of various species with a source diameter large enough to illuminate the entire entrance grid diameter of the LIMS. The ion source and calibration apparatus are sketched in Fig. 4. Electrons produced by the filament generate ions by impact ionization of gases. The ions drift toward the screen under the influence of a weak axial electric field. As the ions approach the screen, they come under the influence of the extractor potential. The beam of ions exits the output grid with a final energy determined by the value of the anode potential.

The LIMS instrument was mounted on a motor-driven tilting fixture so that the instrument could be rotated relative to the beam in order to determine the angular response. A Faraday cup was attached to a swing arm and could be positioned in front of the LIMS entrance aperture in order to monitor the beam current. The entire apparatus was operated under vacuum at 10^{-6} Torr.

The ion mass response of the LIMS was measured by plotting the detector counting rate as a function of the post-acceleration potential. For this measurement the ion-beam energy was held constant and the retarding

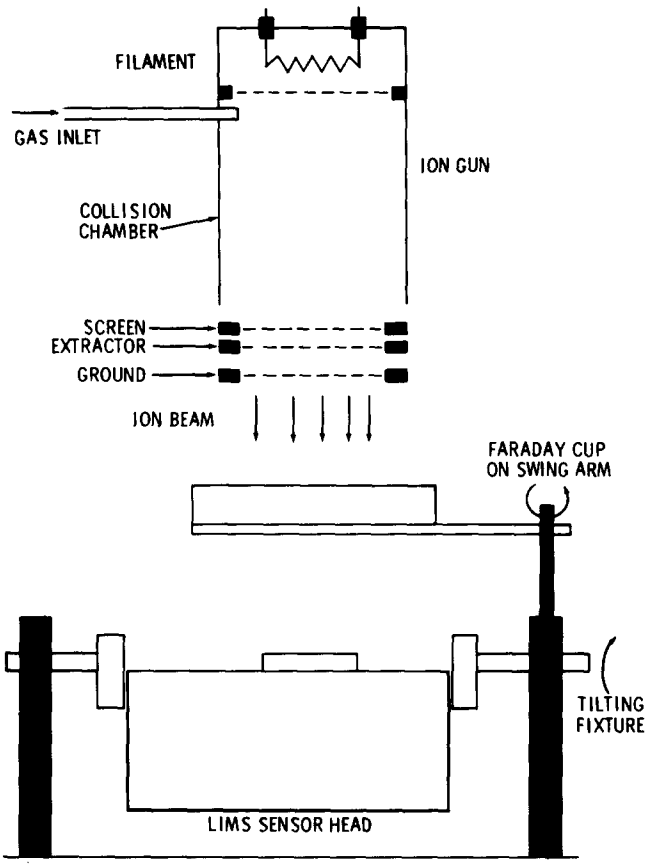

FIG. 4. Sketch of the calibration apparatus used to measure the instrument parameters mass resolution, mass analyzer constant, effective area, and angular response.

potential was fixed at 0 V. Hydrogen gas was introduced into the ion gun from an external source. A typical result is shown in Fig. 5. The prominent peaks, reading from right to left, are H^+ (m/q = 1), H_2^+ (m/q = 2), and a peak at m/q = 3 which is a combination of H_3^+ and HD^+. At the high-mass end of the scale are seen peaks at m/q = 18 which is the ever-present water vapor ion, and a high-mass peak centered at m/q = 30 which is actually unresolved atmospheric ions N_2^+, NO^+, and O_2^+ at m/q = 28, 30, and 32.

From these data the mass resolution was determined to be 0.1 and the mass analyzer constant, or the voltage required to focus ions with m/q = 1 was found to be 965. The total ion-beam current was measured before and after the mass scan, and with these data the effective area A_e was computed to be $A_e = 2.0 \times 10^{-3}$ cm^2.

The angular response of the instrument was measured by plotting the counting rate as a function of angle as the instrument was rotated in the beam. Tests were done for various ion masses and for various ion energies ranging from 5 to 50 eV. Angular scans were made in both the focusing axis and in the nonfocusing axis. The solid angle, Ω, was computed for each ion mass and energy by constructing normalized response contours, transforming from calibration angle space to polar coordinate space, and computing Ω with a numerical evaluation of the integral

$$\Omega = \int R(\Theta, \Phi) d\Omega, \tag{8}$$

where $R(\Theta, \Phi)$ is the response function normalized to unity.

Representative plots of the measured angular response functions are shown in Fig. 6 and illustrate several of the points discussed earlier in the section on the LIMS design. For the same energy and mass, the angular response for the focusing axis is always wider than the response for the nonfocusing axis. The second point is that as the ion energy is increased, the angular response narrows. Finally, as the ion mass is increased for a fixed ion energy, the angular response narrows as well. All of these effects are predicted both qualitatively and quantitatively by Eq. (7) and by consideration of the fixed geometrical limits of the maximum angular departure from the central ray of the ion beam at the entrance to the mass spectrometer. The computed values of Ω as a function of ion energy for m/q = 1, 2, and 18 are shown in Fig. 7. The extrapolated portions of the curve are based on the geometrical limits of the entrance grid structure which defines the solid angle response in the limit as the incident ion energy approaches 0 eV. These curves show the same trends as do the angular scan data; that is, the decrease in the instrument solid angle response with increasing ion energy and mass.

IV. FLIGHT CONFIGURATION OF THE LIMS

The requirement that the LIMS be sensitive to the directional properties of the plasma distribution dictated that multiple analyzers viewing different directions would be needed. As a minimum, the instrument had to be able to sample the plasma characteristics in directions parallel and anti-parallel to each of three orthogonal directions. For an inertially stabilized sensing platform this would imply that six separate analyzers would be required. However, the observing platform was spinning and one analyzer could view four of the required six directions at points in the spin separated by 90°. The flight version

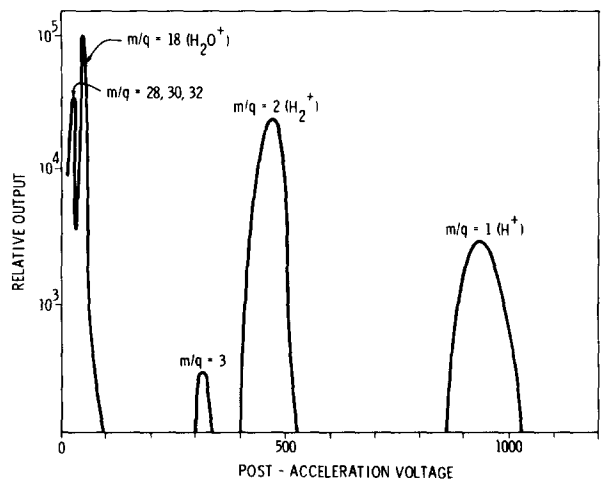

FIG. 5. A mass analyzer scan of the LIMS obtained from the calibration apparatus shown in Fig. 5 above.

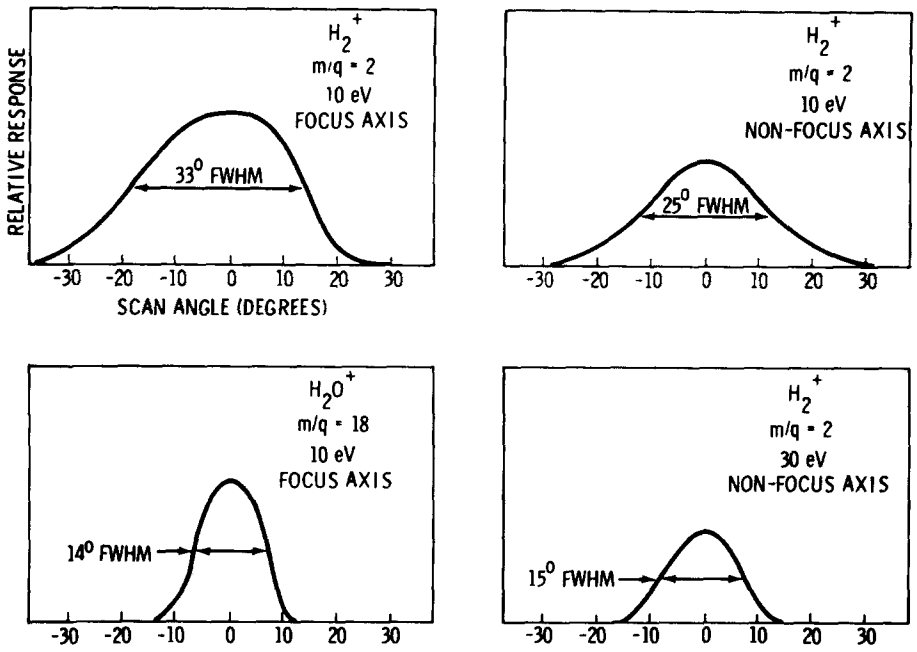

FIG. 6. Data from angular sensitivity measurements of the LIMS. The curves are characterized by their full width at half-maximum (FWHM).

of the LIMS then consisted of three identical sensor heads and a central electronics package for control and data interfacing. The sensor heads each contained a retarding grid assembly, a magnetic ion mass spectrometer, and a channel electron multiplier assembly as previously described. The sensor heads also contained power supplies to furnish the channel electron multiplier bias voltage, the post-acceleration voltage, and the retarding potential voltage. A pulse amplifier and discriminator conditioned the channel multiplier pulse signals. The central electronics package contained all of the digital circuitry necessary for accumulating the pulses and transferring the accumulated count to the spacecraft telemetry system for transmission. This package also received and decoded commands from the spacecraft command decoder and generated the timing and voltage reference signals necessary for the various retarding potential and mass analysis sequences of the instrument.

The SCATHA spacecraft was spin-stabilized with the spin axis maintained in the orbit plane and perpendicular to the satellite-Sun line to within 5°. The three sensor heads were placed on the spacecraft such that sensor head #1 viewed perpendicular to the spin axis while sensor heads #2 and #3 viewed parallel and anti-parallel to the spin axis.

V. FLIGHT DATA

This section will present some examples of flight data from the LIMS on the SCATHA satellite in the on-orbit

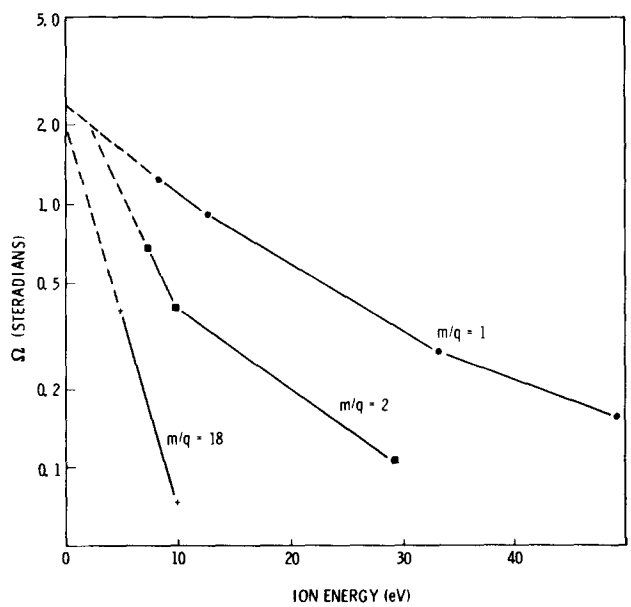

FIG. 7. Computed values of the solid angle response Ω in steradians as a function of ion energy and mass.

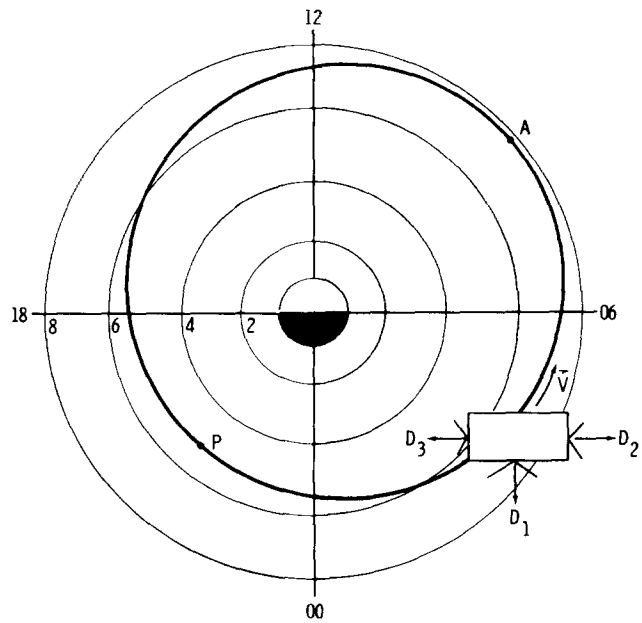

FIG. 8. Geometry of the SCATHA satellite orbit and the sensor head look directions, D_1, D_2, and D_3. The radial coordinate is units of Earth radii R_e ($1R_e$ = 6378 km) and the aximuthal coordinate is local time in hours.

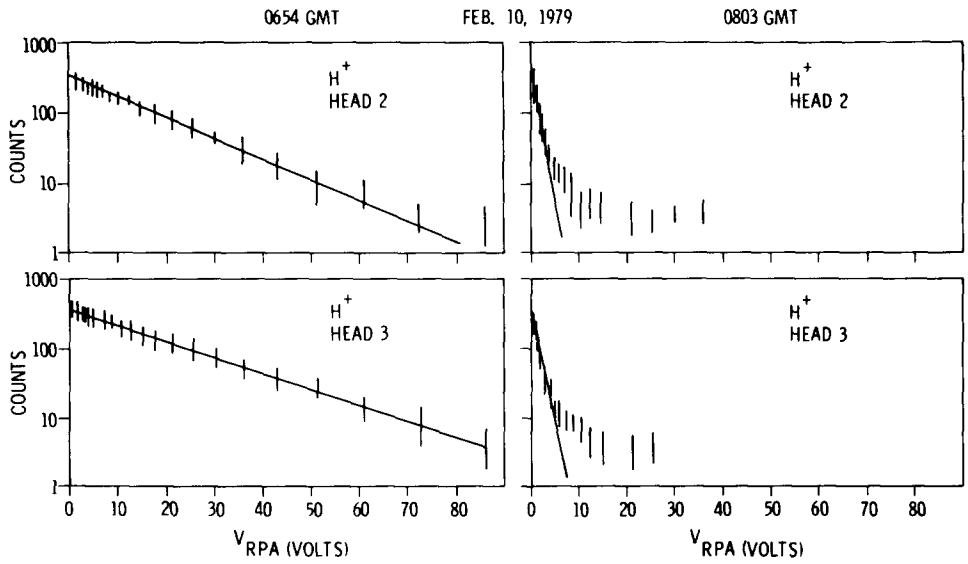

FIG. 9. Examples of retarding potential analyses to determine the plasma temperatures.

configuration. Though not intended as a comprehensive data survey, this presentation will nonetheless illustrate how the plasma analysis capability designed into the instrument was employed to measure the space plasma parameters. The orbit and spacecraft geometry is shown in Fig. 8. The orbit was elliptical with perigee at $5.3R_e$ ($1R_e$ = 6378 km) and apogee at $7.8R_e$. With the spacecraft attitude and spin maintained as shown and as discussed earlier, the three sensor heads formed sets of orthogonal triads with orientations favorable to studying plasma flows in the orbit plane as well as plasma anisotropies and net flows relative to the magnetic-field lines.

Figure 9 shows examples of measurements of the energy distributions, or temperatures, of the low-energy plasma. For these data the mass analyzer was set for H^+ ions, and the plots are counts per accumulation interval (log scale) as a function of RPA voltage. The four panels are data from sensor heads 2 and 3 at two different times. The straight-line fits to the data indicate that the plasma distribution function is well represented as a Maxwellian, and the temperature of the plasma is determined by computing the slope of the line. The two left-hand panels show a case of relatively "warm" plasma with a temperature of 17 eV, while the two right-hand panels show a considerably less energetic population with a temperature of 1.3 eV.

The presence of a strong plasma flow is revealed in the data shown in Fig. 10. The geometry is shown at the top of the figure, with the satellite near 1800 local time. In the right-hand panel, the data from sensor heads 2 and 3 show no modulation with spin, and the flux in sensor 2 is a factor of 2 larger than that in sensor 3. The sensor 1 data (left-hand panel) show 2 maxima per spin with a ratio of the two maxima of 6.5 : 1. The double maximum is indicative of a plasma distribution that is of greater intensity perpendicular to the magnetic-field lines, and the inequality in the two maxima is indicative that this nonisotropic plasma distribution is flowing relative to the spacecraft. Retarding potential analysis showed that the plasma temperature was 3 eV with a density of 1 ion/cm^3. Analysis of the flux ratios in the four directions, the directions of the sensor 1 maxima, and the directions of sensors 2 and 3, resulted in a computed flow velocity relative to the spacecraft of 13.4 km/s.

The mass identification capability of the LIMS is illustrated by the two bottom panels of Fig. 10. Here the instrument was in the density, or mass scan mode. At 0400 the satellite was in a region of relatively high He^+ concentration, a region where the plasma was of ionospheric origin. By 0426, however, the relative He^+ concentration had decreased almost an order of magnitude.

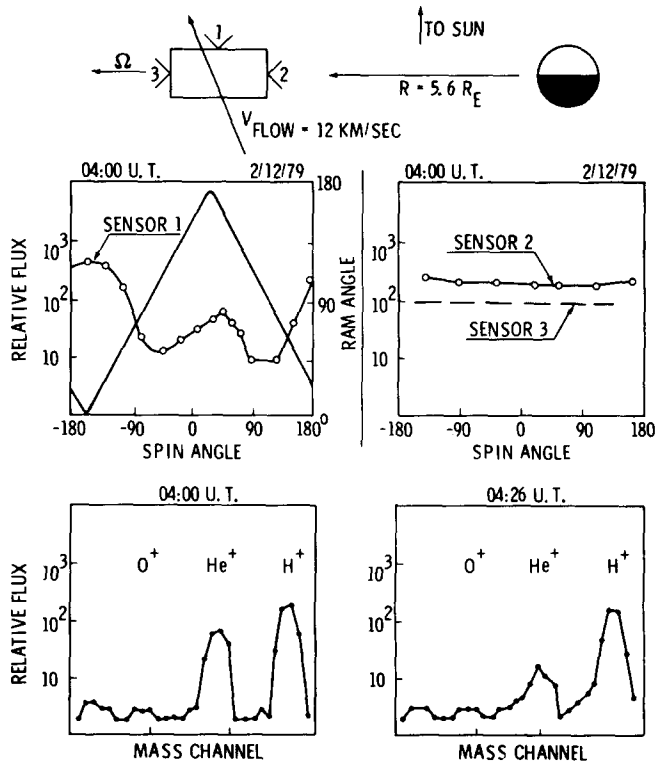

FIG. 10. An example of a LIMS measurement of a convecting nonisotropic plasma distribution.

The plasma flow discussed above apparently convected a plasma boundary past the satellite so that the satellite was in a region called the plasma sheet where the He^+/H^+ ratio is much lower due to the solar wind origin of this plasma. It should be remarked that there was no dramatic change in either the total density or temperature of the plasma, illustrating the importance of mass composition analysis to understanding the overall significance of the plasma measurements.

ACKNOWLEDGMENTS

The LIMS instrument was a cooperative effort between the Magnetospheric Physics Branch at the NASA/Marshall Space Flight Center and the Lockheed Palo Alto Research Laboratories. Special thanks are due to Dr. R. G. Johnson, Dr. J. B. Reagan, Dr. R. D. Sharp, and J. D. Matthews for their contributions in development of the central electronics package. In Huntsville, W. L. Chisholm of MSFC and Ron Eaks and John Medlin of the University of Alabama in Huntsville made invaluable contributions in the areas of mechanical design and fabrication. This work was supported in part by NASA/OSS SR&T Grants 170-36-55 and 385-36-01.

[1] D. L. Carpenter, J. Geophys. Res. **71,** 693 (1968).
[2] D. L. Carpenter, J. Geophys. Res. **75,** 3837 (1970).
[3] C. R. Chappell, Rev. Geophys. Space Phys. **10,** 951 (1972).
[4] P. M. Banks and G. Kockarts, *Aeronomy* (Academic, New York, 1973), Part A, Chap. 18.
[5] C. R. Chappell, C. R. Baugher, and J. L. Horwitz, Rev. Geophys. Space Phys. **18,** 853 (1980).
[6] J. L. Horwitz and C. R. Chappell, J. Geophys. Res. **84,** 7075 (1979).
[7] W. H. Bennett, J. Appl. Phys. **21,** 143 (1950).
[8] W. Paul and H. Steinwedel, Z. Naturforsch. **8a,** 448 (1953).
[9] S. Penner, Rev. Sci. Instrum. **32,** 150 (1961).
[10] S. A. Fields, J. L. Burch, and W. A. Oran, Rev. Sci. Instrum. **48,** 1076 (1977).